Large-grained (111)-oriented $Si/Al/SiO_2$ structures formed by diffusion-controlled Al-induced layer exchange

Ryohei Numata[a], Kaoru Toko[a,*], Noritaka Usami[b], and Takashi Suemasu[a]

[a] *Institute of Applied Physics, University of Tsukuba, Tsukuba, Ibaraki 305-8573, Japan*

[b] *Materials, Phys. and Energy Eng., Nagoya Univ., Aichi 464-8603, Japan*

* Corresponding author: Kaoru Toko

Institute of Applied Physics, University of Tsukuba,

1-1-1 Tennohdai, Tsukuba, Ibaraki 305-8573, Japan

Phone: +81-29-853-5472, Fax: +81-29-853-5205

E-mail: toko@bk.tsukuba.ac.jp

Abstract

We investigated inverted Al-induced crystallization (AIC) technique of amorphous Si films (thickness: 50-100 nm) for the formation of polycrystalline Si films on Al coated glass substrates at low-temperature (< 500 ˚C). A SiO_2 interlayer was inserted in between Al and Si layers in order to control the Al-Si diffusion rate. As a result, the crystal orientation of the AIC-Si layer strongly depend on the thickness of the SiO_2 interlayer: thin (1 nm) interlayer provided (100) orientation while thick (10 nm) interlayer provided (111) orientation. Meanwhile, the thicker the SiO_2 interlayer, the larger the grain size of the AIC-Si layer. In particular, for a sample with 10-nm-thick SiO_2 interlayer, the (111) orientation fraction reached 99% and the average grain size over 50-μm diameters. This AIC-Si layer holds promise as epitaxial templates for light-absorption layers of thin-film solar cells, as well as for functional silicide materials.

Keywords: A1.Crystal orientation; A2.Solid phase crystallization; B1.Polycrystalline films;

37 **1. Introduction**

38 The preparation techniques of high-quality polycrystalline Si (poly-Si) films on
39 insulators are essential for thin-film transistor (TFT) and highly-efficient thin-film solar
40 cells. For fabricating poly-Si films on inexpensive glass substrates (softening
41 temperature: 550 ˚C), many low-temperature crystallization techniques have been
42 developed [1-3]. Among them, the study of Al-induced crystallization (AIC) technique
43 is recently accelerated, which enables large-grained (diameters: 10-100 μm) poly-Si
44 films at relatively low temperatures (420-550 ˚C) [4-24]. Moreover, the crystal
45 orientations of the poly-Si films can be controlled to either (111) or (100) plane by
46 modulating the Al/Si thickness, the annealing temperatures, and the interlayer thickness
47 between Al and Si layer [10-18].

48 For practical solar-cell application, a conducting layer, which works as a
49 bottom electrode, is required in between the poly-Si film and the glass substrate [25].
50 Lee *et al.* achieved preferentially (100)-oriented Si layers on conducting layer
51 (Al-doped ZnO) coated glass substrates using the AIC technique [26]. (111)-oriented
52 poly-Si on a conducting layer is desirable as epitaxial templates for advanced-functional
53 silicide materials [27-29]. To achieve this, an inverted-AIC technique has been studied
54 [30-32]. In this technique, the initial structure is Al/amorphous-Si (a-Si)/substrate which

55 in contrast to the conventional AIC structure: a-Si/Al/substrate. After annealing, an Al

56 conducting layer was formed under the poly-Si film through the layer exchange process.

57 Previously we found that the crystal orientation of the poly-Si layer, formed by the

58 inverted AIC, strongly depends on the Al/Si thickness [33]. The sample with the

59 50-nm-thick Si and Al layers provided highly (111)-oriented Si layer with the average

60 grain diameter of 20 μm. However, the Al/Si interlayer formation process was not

61 optimized, which is one of the important parameters for the AIC [11-18]. Hence, there is

62 the possibility to improve the crystal quality of the inverted-AIC-Si layer. In this paper,

63 we focused on the SiO_2 interlayer formation process between Al and Si layers in the

64 inverted-AIC. As a result, we accomplished the enhancement of the average grain size

65 over 50-μm diameters.

66

67 **2. Experimental**

68 Amorphous Si films (thickness: 50 nm and 100 nm) were prepared on SiO_2

69 glass substrates. Subsequently, SiO_2 interlayers (thickness: 1 nm, 2 nm and 10 nm) were

70 formed on the Si films: 1-nm-thick interlayer was formed by dipping the sample in

71 APM solutions (NH_4OH: H_2O_2: H_2O = 1: 1: 10) for 30 min at 80 ˚C; 2-nm-thick and

72 10-nm-thick SiO_2 interlayers were prepared by RF magnetron sputtering. After that, Al

73 films with the same thickness as the a-Si films were prepared on the SiO_2 membranes.

74 Si and Al depositions were carried out at room temperature by RF magnetron sputtering

75 with Ar plasma. Finally all samples were annealed in N_2 ambient at 375 ˚C for 100 h,

76 400-425 ˚C for 50 h, and 450-500 ˚C for 10 h. The scheme of the sample structure is

77 shown in Fig. 1. The surface morphology and crystal orientation of the AIC-Si layers

78 were characterized by Nomarski optical microscopy and electron backscatter diffraction

79 (EBSD) analysis, respectively.

80

81 **3. Results and discussion**

82 Fig. 2 shows the growth evolution of AIC-Si observed by Nomarski optical

83 microscopy. For this sample, the Al and Si thickness (Al/Si thickness) is 100 nm, the

84 SiO_2 interlayer thickness is 1 nm, and the annealing condition is 450 ˚C for 10 h. In

85 these micrographs, the dark area indicates crystallized Si and the bright-color area Al.

86 These suggest that the Si atoms diffuse to the top surface, grow laterally, and cover the

87 whole surface of the sample during the annealing. This growth morphology is almost

88 the same as the conventional AIC process [5-18].

89 The dependence of the SiO_2 interlayer thickness on the crystal orientation of

90 the AIC-Si layers was investigated using EBSD measurements. The results for the

91 100-nm-thick sample annealed at 450 ˚C for 10 h are shown in Fig. 3(a)-(c). These
92 orientation mappings indicate that the crystal orientation strongly depends on the SiO_2
93 interlayer thickness. The area fractions of (100) and (111) orientations were derived by
94 EBSD analysis. Fig. 3(d) clearly indicates that the (111) fraction increases with
95 increasing the SiO_2 interlayer thickness; in contrast, the (100) fraction decreases with
96 increasing the SiO_2 interlayer thickness. This trend is the same with the conventional
97 AIC [18], and can be explained as follows. The interlayer-thickness dependence of
98 crystal orientation of AIC-Si is probably attributed to the different growth rates between
99 Si (100) and (111). When the SiO_2 interlayer is thick, the diffusion rate of Si atoms into
100 Al is slow. This results in the dominant (111) orientation, because (111) is a stable plane
101 [34]. In contrast, when the SiO_2 interlayer is thin, the diffusion rate of Si atoms into Al
102 is fast. Because the (111) growth rate is much lower than the (100) growth rate [35],
103 (111) plane cannot follow the fast diffusion rate. As a result, (100) orientation is
104 dominant when the SiO_2 interlayer is thin. Therefore, we found that the thick interlayer
105 is preferable for (111)-oriented Si layers.
106 Regarding the Al/Si thickness, we have found that the 50-nm-thick sample
107 provides higher (111) fraction than the samples with thick (≥ 100 nm) Al/Si films [33].
108 Therefore, we prepared 50-nm-thick samples with thick SiO_2 interlayers. The EBSD

109 mappings, along the normal direction (ND) with respect to the substrates, were
110 summarized in Fig. 4 as a matrix of annealing temperature and the SiO_2 interlayer
111 thickness. The AIC-Si layers are preferentially oriented to (111) due to the thin (50 nm)
112 Al/Si layers except the three blanks in Fig. 4. For the 475 ˚C (10 h) annealed sample
113 with a 1-nm-thick interlayer, the interlayer was broken by the high temperature
114 annealing, which resulted in an Al/Si mixed layer with random-oriented small grains.
115 Meanwhile, for the sample with a 10-nm-thick interlayer, AIC did not occur at 425 ˚C
116 and 450 ˚C for 10 h because of the thick interlayer, which is a diffusion barrier for Si
117 and Al atoms. The high temperature annealing (475 ˚C) facilitated the diffusion, and
118 enabled the AIC of the sample as shown in Fig. 4(f). In order to evaluate the grain size,
119 we obtained EBSD orientation mappings along the transverse (in-plane) directions (TD)
120 with respect to the sample surfaces. The results are shown in Fig. 5, which correspond
121 to the ND mappings of the same areas shown in Fig. 4. The black solid lines in these
122 images indicate random grain boundaries, which were drawn by EBSD analysis. For all
123 samples, the grain sizes are estimated over 10-μm diameters. In particular, the grain
124 sizes in Fig. 5(c) and (f) are larger than those in the other samples.

125 EBSD analysis derived the area-fraction of (111) orientation and the grain size
126 from the orientation mappings in Fig. 4 and 5. The results are illustrated in Fig. 6(a) and

127 (b), respectively. By definition, the (111) fraction contains planes that are tilted within
128 15° of the exact (111) plane. The (111) fraction clearly increases with decreasing
129 annealing temperature, and reaches as high as 99% for all of the samples with 1-nm,
130 2-nm, and 10-nm-thick SiO_2 interlayers. Meanwhile, Fig. 6(b) indicates that the grain
131 size increases with thickening the SiO_2 interlayer. In general, the grain size is
132 determined by nucleation rate and lateral growth rate [36]. The nucleation occurs as a
133 result of a supersaturation of Al with Si diffused from the a-Si layer, after that, Si atoms
134 migrating in Al adhere to the Si nucleus, which causes the lateral growth [12]. Hence,
135 the interlayer thickness dependent grain size can be explained as follows. The thicker
136 SiO_2 interlayer yields a lower diffusion rate of Si atoms into Al, which results in a lower
137 nucleation rate. On the other hand, the migration rate of Si atoms in Al is constant with
138 the SiO_2 interlayer thickness. Considering that, when the Si nucleation rate is low, Si
139 atoms in Al have much time to migrate and adhere to the Si nucleus before the other
140 nucleation occurs. Therefore, the thicker interlayer enables a wider margin between the
141 nucleation rate and lateral growth rate, which resulted in the larger grain size.

142 On the other hand, Fig. 6(b) also indicates that the grain size increases with
143 decreasing annealing temperature. Mina *et al.* indicates that the higher annealing
144 temperature yields a higher (100) fraction because of the high diffusion rate of Si atoms

145 [13]. On the other hand, concerning the grain size, Sarikov *et al*. theoretically
146 demonstrated that the higher annealing temperature yields a higher nucleation density
147 because of the reduction of the Si supersaturation level in Al [12]. Therefore, the crystal
148 orientation and grain size of AIC-Si are determined by the balance of the interlayer
149 thickness and annealing temperature. Consequently, the 475 ˚C annealed sample with
150 10-nm-thick interlayer provides the largest grain size of 57 μm diameters.
151

152 **4. Conclusion**

153 The inverted Al-induced crystallization (AIC) of a-Si film was investigated
154 focusing on the SiO_2 interlayer thickness to obtain a larger grain size than the
155 conventional inverted AIC-Si. We found that the grain size and crystal orientation of the
156 inverted AIC-Si layers strongly depended on the SiO_2 interlayer thickness: The thicker
157 the interlayer, the larger the grain size and the higher (111) orientation fraction. By
158 combining the thin Al/Si films (50 nm each) and the thick (10 nm) SiO_2 interlayer, the
159 average grain size over 50-μm diameters and (111) orientation fraction reached as high
160 as 99%. Therefore, the effects of the SiO_2 interlayer on inverted-AIC-Si were clarified,
161 which enabled more than doubled size of (111)-oriented grains compared to the
162 conventional technique. This large-grained (111)-oriented poly-Si film on a conducting

163 layer holds promise as epitaxial seeds for advanced functional silicide materials.

164

165 **Acknowledgements**

166 This work was partially supported by Yazaki Memorial Foundation for Science

167 and Technology, and was performed under the Inter-University Cooperative Research

168 Program of the Advanced Research Center of Metallic Glasses, Tohoku University.

169

170 **References**

171 [1] C. Hayzelden and J.L. Batstone, J. Appl. Phys. 73 (1993) 8279.

172 [2] K. Toko, H. Kanno, A. Kenjo, T. Sadoh, T. Asano, M. Miyao, Appl. Phys. Lett. 91

173 (2007) 042111.

174 [3] Y. Sugawara, Y. Uraoka, H. Yano, T. Hatayama, T. Fuyuki, T. Nakamura, S. Toda, H.

175 Koaizawa, A. Mumura, K. Suzuki, Appl. Phys. Lett. 91(2007) 203518.

176 [4] G.Radnoczi, A. Robertsson, H. T. G. Hentzell, S. F. Gong, M. A. Hasan, J. Appl.

177 Phys. 69 (1991) 6394.

178 [5] O. Nast, T. Puzzer, L.M. Koschier, A.B. Sproul, S.R. Wenham, Appl. Phys. Lett. 73

179 (1998) 3214.

180 [6] P. Widenborg, A. G. Aberle, J. Cryst. Growth 242 (2002) 270.

181 [7] Y. Sugimoto, N. Takata, T. Hirota, K. Ikeda, F. Yoshida, H. Nakashima, H.

182 Nakashima, Jpn. J. Appl. Phys. 44 (2005) 4770.

183 [8] J.Y. Wang, Z.M. Wang, and E.J. Mittemeijer, J. Appl. Phys. 102 (2007) 113523.

184 [9] B.I. Birajdar, T. Antesberger, B. Butz, M. Stutzmann, E. Spiecker, Scripta Materialia

185 66 (2012) 550.

186 [10] H. Jeong, S. Boo, Int. J. Photoenergy 2012 (2012) 593257.

187 [11] M. Kurosawa, N. Kawabata, T. Sadoh, M. Miyao, Appl. Phys. Lett. 95 (2009)

188 132103.

189 [12] A. Sarikov, J. Schneider, J. Berghold, M. Muske, I. Sieber, S. Gall, W. Fuhs, J.

190 Appl. Phys. 107 (2010) 114318.

191 [13] M. Jung, A. Okada, T. Saito, T. Suemasu, N. Usami, Appl. Phys. Express 3 (2010)

192 095803.

193 [14] O. Ebil, R. Aparicio, R. Birkmire, Thin Solid Films 519 (2010) 178.

194 [15] M. Kurosawa, K. Toko, N. Kawabata, T. Sadoh, M. Miyao, Solid-State Electron. 60

195 (2011) 7.

196 [16] C. C. Peng, C. K. Chung, J. F. Lin, Acta Materialia 59 (2011) 6093.

197 [17] S. Y. Wei, S. M. Yu, L. C. Yu, W. C. Sun, C. K. Hsieh, T. S. Lin, C. H. Tsai, F. R.

198 Chen, Cryst. Eng. Comm. 14 (2011) 4967.

199 [18] A. Okada, K. Toko, K. O. Hara, N. Usami, T. Suemasu, J. Cryst. Growth 356

200 (2012) 65.

201 [19] D. Dimova-Malinovska, O. Angelov, M. Sendova-Vassileva, M. Kamenova, J. C.

202 Pivin, Thin Solid Films 451-452 (2004) 303.

203 [20] S. K. Patil, Z. Celik-Butler, D. P. Butler, Thin Solid Films 519 (2010) 479.

204 [21] T. Wang, H. Yan, M. Zhang, X. song, Q. Pan, T. He, Z. Hu, H. Jia, Y. Mai, Appl.

205 Surf. Sci. 264 (2013) 11.

206 [22] K. Toko, M. Kurosawa, N. Saitoh, N. Yoshizawa, N. Usami, M. Miyao, T. Suemasu,
207 Appl. Phys. Lett. 101 (2012) 072106.
208 [23] I. Gordon, L. Carnel, D.V. Gestel, G. Beaucarne, J. Poortmans, Thin Solid Films
209 516 (2008) 6984.
210 [24] B.R. Wu, S.Y. Lo, D.S. Wuu, S.L. Ou, H.Y. Mao, J.H. Wang, R.H. Horng, Thin
211 Solid Films 520 (2012) 5860.
212 [25] C. Becker, E. Conrad, P. Dogan, F. Fenske, B. Gorka, T. Hänel, K. Y. Lee, B. Rau,
213 F. Ruske, T. Weber, Sol. Energy Mater. Sol. Cells 93 (2009) 855.
214 [26] K. Y. Lee, M. Muske, I. Gordon, M. Berginski, J. D'Haen, J. Hüpkes, S. Gall, B.
215 Rech, Thin Solid Films 516 (2008) 6869.
216 [27] D. Tsukada, Y. Matsumoto, R. Sasaki, M. Takeishi, T. Saito, N. Usami, T. Suemasu,
217 Appl. Phys. Express 2 (2009) 051601.
218 [28] M. Suzuno, T. Koizumi, T. Suemasu, Appl. Phys. Lett. 94 (2009) 213509.
219 [29] Y. Ando, K. Hamaya, K. Kasahara, Y. Kishi, K. Ueda, K. Sawano, T. Sadoh, M.
220 Miyao, Appl. Phys. Lett. 94 (2009) 182105.
221 [30] G. Ekanayake, T. Quinn, H. S. Reehal, J. Cryst. Growth 293 (2006) 351.
222 [31] C. Jaeger, T. Matsui, M. Takeuchi, M. Karasawa, M. Kondo, M. Stutzmann, Jpn. J.
223 Appl. Phys. 49 (2010) 112301.

224 [32] H. Kuraseko, N. Orita, H. Koaizawa, M. Kondo, Appl. Phys. Express 2 (2009)
225 015501.
226 [33] R. Numata, K. Toko, N. Saitoh, N. Yoshizawa, N. Usami, T. Suemasu, Crystal
227 Growth and Design 13 (2013) 1767.
228 [34] A.A. Stekolnikov, J. Furthmuller, F. Bechstedt, Physical Review B 65 (2002)
229 115318.
230 [35] L. Csepregi, E.F. Kennedy, J.W. Mayer, J. Appl. Phys. 49 (1978) 3906.
231 [36] C. Spinella, S. Lombardo, F. Priolo, J. Appl. Phys. 84 (1998) 5383.
232

233 **Figure captions**

234

235 **Fig. 1.** Scheme of the layer exchange growth in the inverted-AIC of a-Si.

236

237 **Fig. 2.** Nomarski optical micrographs of the 100-nm-thick Al/Si sample with 1-nm-thick

238 SiO_2 interlayer, annealed at 450 ^oC for (a) 0 h, (b) 1 h, and (c) 10 h.

239

240 **Fig. 3.** EBSD (ND) images of the grown 100-nm-thick Al/Si sample with (a) 1 nm, (b) 2

241 nm, and (c) 10 nm SiO_2 interlayers. (d) Area fraction of (111) and (100) orientations as a

242 function of the SiO_2 interlayer thickness. The inserted color key corresponds to crystal

243 orientations.

244

245 **Fig. 4.** EBSD (ND) images of the 50-nm-thick Al/Si sample after annealing summarized

246 as a matrix composed of annealing temperature (425, 450 and 475 ^oC) and SiO_2

247 interlayer thickness (1, 2 and 10 nm).

248

249 **Fig. 5.** EBSD (TD) images of the 50-nm-thick Al/Si sample after annealing summarized

250 as a matrix composed of annealing temperature (425, 450 and 475 ^oC) and SiO_2

251 interlayer thickness (1, 2 and 10 nm). Each image corresponds to the ND EBSD images

252 shown in Fig. 4.

253

254 **Fig. 6.** (a) (111) orientation fraction and (b) grain size of the 50-nm-thick Al/Si samples

255 with SiO_2 interlayers (1, 2, 10-nm thickness) as a function of annealing temperature.

256

257

258

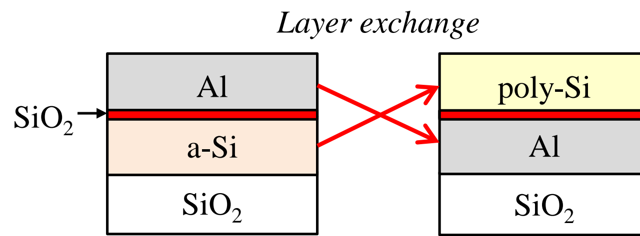

Fig. 1

259

260

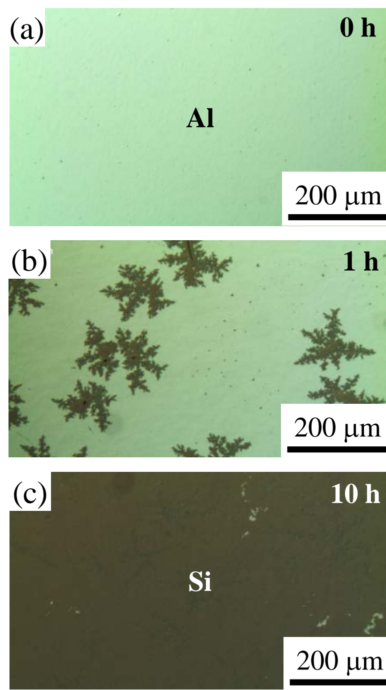

Fig. 2

261

262

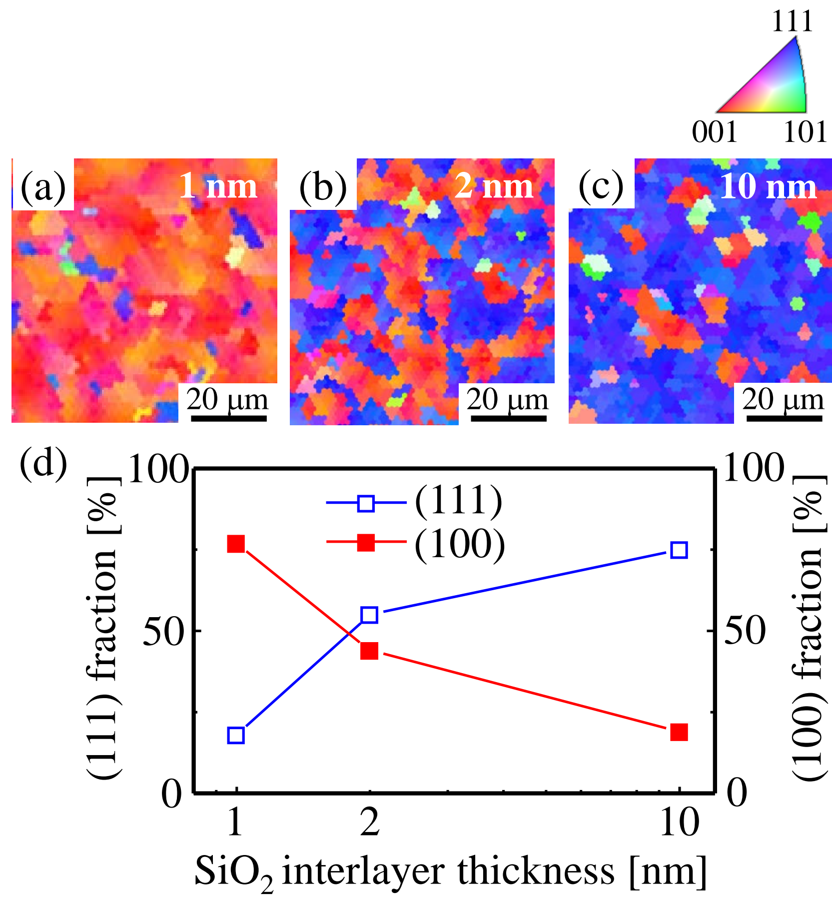

Fig. 3

263

264

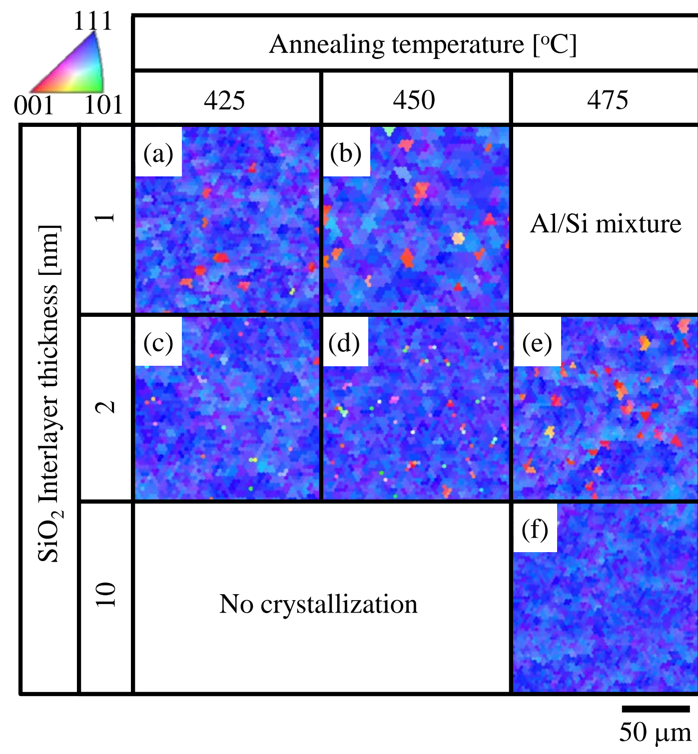

Fig. 4

265

266

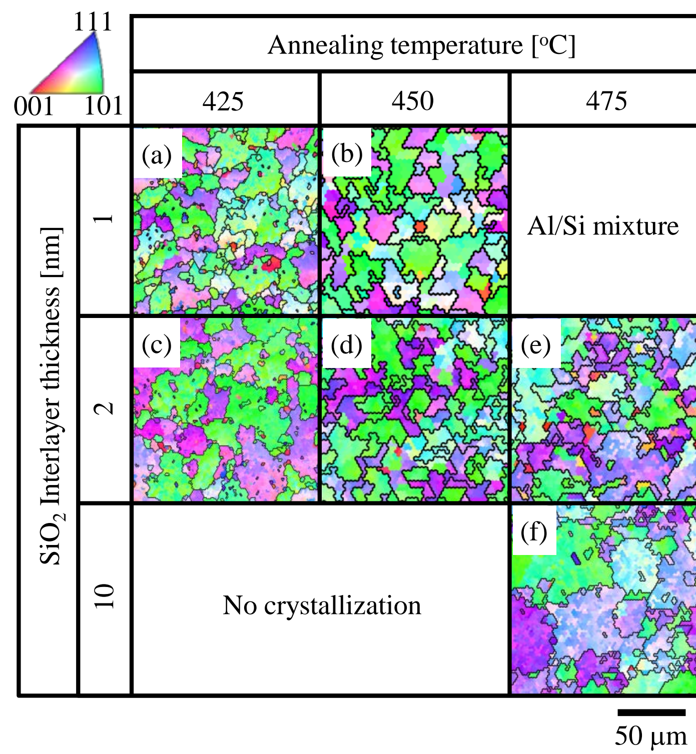

Fig. 5

267

268

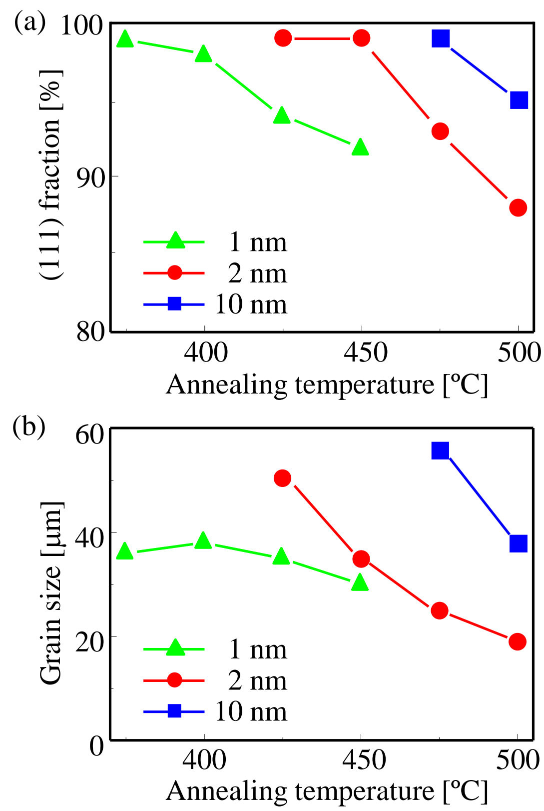

Fig. 6